Basic Control Principles of Omnidirectional Wireless Power Transfer

Cheng Zhang, *Student Member, IEEE*, Deyan Lin, *Member, IEEE*, and S. Y. Hui, *Fellow, IEEE*

***Abstract*—This paper presents the basic control principles of omnidirectional wireless power transfer (WPT) based on the current amplitude control. The principles involve 1) an "omnidirectional" scanning process for detecting the power requirements in a 3-D space and 2) a "directional" power flow control for focusing the wireless power toward the targeted areas. Such principles apply to any WPT system comprising three orthogonal transmitter coils and multiple receivers with coil resonators. A current amplitude control method capable of generating a magnetic vector at a set of points evenly distributed on a spherical surface is explained. Based on the voltage and the current information in the transmitter circuit, the power involved in each vector over the spherical surface can be obtained. By scanning the vector over the spherical surface, the collective power flow requirements for the targeted loads can be determined. Based on the power requirements for the vectors over the spherical surface, a weighted time-sharing scheme is adopted to focus the wireless power toward the targeted areas. This method has been successfully applied to a hardware prototype. Both theoretical and experimental results are included to confirm these principles.**

***Index Terms*—Contactless power, omnidirectional power, wireless power transfer.**

I. Introduction

With the developments of the Ampere's law in 1826 and the Faraday's law in 1831, early scientists and inventors, such as Tesla [1], and Hutin and Leblanc [2] pioneered wireless power transfer (WPT) research in the late 19th century. In particular, Tesla has been recognized as the dominant figure who pioneered the use of magnetic coupling and magnetic resonance for WPT [3]. However, since the early WPT research, a century ago, there were not many applications of WPT in the first half of the 20th century. Although some WPT research emerged again in the field of medical implants in the 1960s, WPT research and developed activities actually became active again in the 1980's when 1) power electronics technology and 2) Litz wire technology became mature and commercially available.

So far, the majority of WPT works involve directional power flow [4]–[8]. Omnidirectional WPT systems have been reported in [9]–[12]. Among them, O'Brien [9] has addressed an omnidirectional WPT system comprising a transmitter with three orthogonal coils and a receiver also with three orthogonal coils (see Fig. 1). In [9], several methods covering 1) periodic switching of the plane of rotation, 2) frequency shift, 3) single-axis amplitude modulation, 4) double-axis amplitude modulation, and 5) wide-band operation have been discussed for omnidirectional magnetic field generation. The use of the double layers of conductive and ferromagnetic materials, which is a concept originally reported in [13] and [14], is also suggested for electromagnetic shielding.

One major contribution of [9] is the explanation for the need for using nonidentical current control for the orthogonal transmitter coils in order to generate omnidirectional magnetic field. Further illustration on this point can also be found in [15]. Some WPT systems using the same orthogonal coils for the transmitter are not truly omnidirectional [10]–[12] because the three transmitter coils are connected in series, and, thus, share the same current. However, two important issues remain unresolved. First, although nonidentical current control can generate

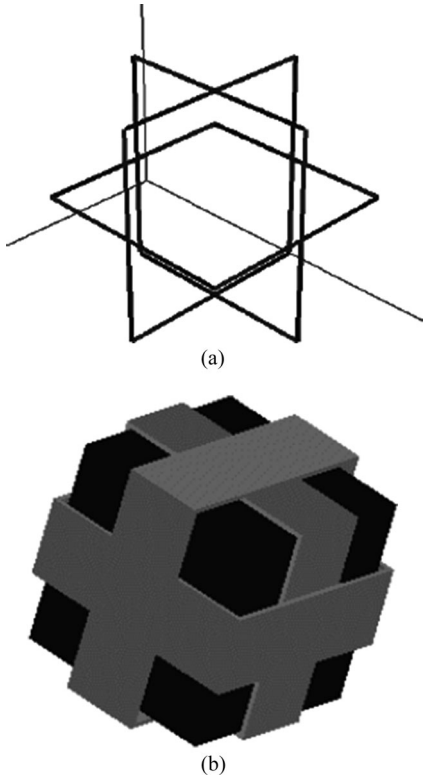

Fig. 1. (a) Transmitter with three orthogonal coils [9]. (b) Receiver with three orthogonal coils wound on a ferrite cube [9].

Manuscript received May 11, 2015; revised July 30, 2015; accepted August 28, 2015. Date of publication September 16, 2015; date of current version January 28, 2016. This work was supported by the Hong Kong Research Grant Council under the Project HKU 17206715, and also by the Philip Wong and Wilson Wong Endowment Fund for the patent application [16]. Recommended for publication by Associate Editor M. A. E. Andersen.

C. Zhang and D. Lin are with the Department of Electrical and Electronic Engineering, The University of Hong Kong, Pokfulam, Hong Kong (e-mail: czhang@eee.hku.hk; deyanlin@eee.hku.hk).

S. Y. Hui is with the Department of Electrical and Electronic Engineering, Imperial College London, London SW7 2AZ, U.K., and also with the Department of Electrical and Electronic Engineering, The University of Hong Kong, Pokfulam, Hong Kong (e-mail: ronhui@eee.hku.hk).

Color versions of one or more of the figures in this paper are available online at http://ieeexplore.ieee.org.

Digital Object Identifier 10.1109/TPEL.2015.2479246

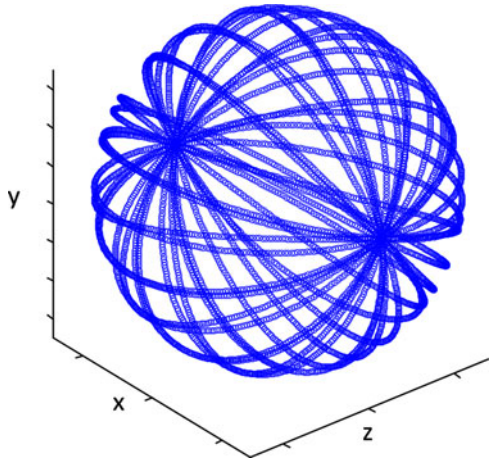

Fig. 2. Trajectory of the equivalent magnetic field vector under a nonidentical current control [9], [15].

an equivalent magnetic field vector that can point in all direction as shown in Fig. 2, there is no guarantee that such vector can point evenly in all directions. For example, the vector density in the two poles of the sphere in Fig. 2 is higher than that in the equatorial region. Therefore, there is a need to develop a new technique to ensure that the magnetic field can be uniformly distributed if necessary. The capability of generating magnetic field with uniform distribution means that the wireless power flow can be truly omnidirectional. Second, a control method is needed to automatically detect the load positions, and, then, focus the power flow directionally to the targeted loads. Directional power flow is more energy efficient than omnidirectional power flow that involves power transfer directed unnecessary to regions without the loads.

In this paper, a new technique that can "omnidirectionally" detect the loads and then focus the power flow "directionally" toward the targeted loads through a weighted time-sharing power control is proposed. It is applied to an omnidirectional WPT system for both single and multiple loads. A new omnidirectional control method that ensures loads to receiver power in any positions in the proximity of the omnidirectional magnetic field is presented. The mathematical theory describing such method is included and proven with practical measurements obtained from a hardware prototype.

II. Basic Control Principles of Omnidirectional Load Detection

In this section, the basic control principles of true omnidirectional WPT are explained with the help of the setup shown in Fig. 3. In the structure of three-orthogonal and cocentered circular coils, the mutual inductances of the three transmitter coils are zero theoretically and negligible in practice. So such mutual inductances can be ignored in the analysis. Nonidentical current control is adopted and so three separate current sources are used in Fig. 3. In practice, a three-phase power inverter can be used to power the three transmitter coils. The power inverter

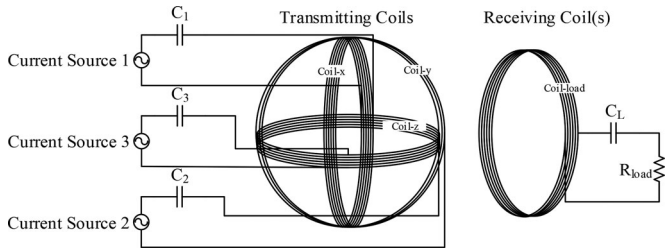

Fig. 3. Three orthogonal coil transmitter structure for omnidirectional wireless energy transfer.

can be operated in either voltage-control mode or current-control mode.

A. Current Vector and Magnetic Field Vector

For a single planar circular coil, the magnetic field at the center of the coil can be obtained from Biot–Savart law

$$\mathbf{B_O} = \frac{\mu_o I}{4\pi r^2}\oint dl \cdot (\hat{\boldsymbol{l}} \times \hat{\boldsymbol{r}}) = \frac{\mu_o I}{2r} \cdot (\hat{\boldsymbol{l}} \times \hat{\boldsymbol{r}}) \qquad (1)$$

where $\hat{\boldsymbol{l}}$ and $\hat{\boldsymbol{r}}$ are the tangential and radial unity vectors of the planar circular coil, respectively. Therefore, vector $\mathbf{B_o}$ is always perpendicular to the coil plane. The magnitude of the magnetic field is always proportional to the current flowing through the coil. This understanding can be extended to the three orthogonal coil situations, where the central magnetic field $\mathbf{B_o}$ can be described as a vectorial sum of three orthogonal vectors with their respective current values multiplied by a coefficient.

Assuming that the three identical circular coils x, y, z are coils placed on yz, xz, and xy planes, respectively, and all three coils are cocentered at the origin, as shown in Fig. 3, the magnetic field vector at the center $\mathbf{B_o}$ equals to the superposition of three component magnetic field vectors from the three coils, $\mathbf{B_x}$, $\mathbf{B_y}$, and $\mathbf{B_z}$

$$\mathbf{B_o} = \mathbf{B_x} + \mathbf{B_y} + \mathbf{B_z} = \frac{\mu_0}{2r}(I_x\hat{\mathbf{i}} + I_y\hat{\mathbf{j}} + I_z\hat{\mathbf{k}}). \qquad (2)$$

From the origin of transmitter coils' Cartesian coordinates, the direction of the resultant magnetic field vector is the same as the vector $(I_x\hat{\mathbf{i}} + I_y\hat{\mathbf{j}} + I_z\hat{\mathbf{k}})$. Therefore, by changing the currents flowing through the coils, the magnetic field can be directed to any directions without moving the physical transmitter coil structures. By varying the three transmitter-coil currents (I_x, I_y, and I_z) under nonidentical current control [9], [15], the resultant magnetic field vector can point (or scan) in different orientations forming the surface of an imaginary sphere as shown in Fig. 2. The next step is to find a way to ensure that the resultant vector can point evenly over the spherical surface because such function allows power to be transferred in a true omnidirectional manner. Note that being able for the vector to point at all directions does not necessarily mean that power must be directed at all directions. It only means that the WPT system has such ability to transfer power at any direction if necessary.

B. Uniformly Distribution Over the Surface of a Sphere

One solution to uniformly distribute vectors on sphere surface comes from J. J. Thompson's problem of electron distributions in an atom, known as the plum pudding model in 1904 [17]. Iterating and solving the coordinates of a number of electrons for the minimum total energy of the system would give a set of uniformly distributed vectors. This idea is adopted in this project. One can predetermine a set of unit vectors that are distributed evenly over the surface of a sphere. Assuming N number of points are used to represent the surface of a sphere, such unity vector set with even distribution is represented as $\mathbf{P_n} = \{\boldsymbol{p_1}, \boldsymbol{p_2}, \boldsymbol{p_3} \ldots \boldsymbol{p_n}\}$ in this paper. The magnitude of any vector in set $\mathbf{P_n}$ is 1

$$|\boldsymbol{p_m}| = 1 \; \forall \boldsymbol{p_m} \in \mathbf{P_n}. \tag{3}$$

The transmitter coils are driven with high-frequency sinusoidal currents in order to transfer power using magnetic coupling and/or magnetic resonance. Since the three orthogonal coils have zero mutual inductance with each other, it is simple to control the driving currents or voltages with the same phase angle, i.e., either 0 phase shift or 180º out of phase. In this situation, the resultant magnetic field vector at the center $\mathbf{B_o}$ can oscillate in any direction which can in turn be controlled by varying the magnitudes of the three coil currents. The omnidirectional magnetic field vector can be controlled by "current-control" mode or "voltage-control" mode. The current-control mode is a direct control approach, while the voltage-control mode is an indirect one.

Under the current-control mode, the three coil currents are controlled current sources. They can be implemented with power inverter with output current control so that the three output currents of the power inverter will follow their respective current reference waveforms. Mathematically, the control current sources can be described as

$$\begin{cases} \boldsymbol{p_m} \in \mathbf{P_n}, m \in [1..n] \\ i_x(t) = C_i \left(\boldsymbol{p_m} \cdot \hat{\mathbf{i}}\right) \sin(\omega t) \\ i_y(t) = C_i \left(\boldsymbol{p_m} \cdot \hat{\mathbf{j}}\right) \sin(\omega t) \\ i_z(t) = C_i \left(\boldsymbol{p_m} \cdot \hat{\mathbf{k}}\right) \sin(\omega t) \end{cases} \tag{4}$$

where C_i is the current amplitude for adjusting the total output power level, ω is the angular frequency of the current sources, and t is the time variable. Therefore

$$\mathbf{B_o} = \frac{\mu_0 C_i \boldsymbol{p_m}}{2r} \sin(\omega t). \tag{5}$$

For the voltage-control mode, the voltage vectors along the three axes are

$$\begin{cases} v_x(t) = C_v \left(\boldsymbol{p_m} \cdot \hat{\mathbf{i}}\right) \sin(\omega t) \\ v_y(t) = C_v \left(\boldsymbol{p_m} \cdot \hat{\mathbf{j}}\right) \sin(\omega t) \\ v_z(t) = C_v \left(\boldsymbol{p_m} \cdot \hat{\mathbf{k}}\right) \sin(\omega t) \end{cases} \tag{6}$$

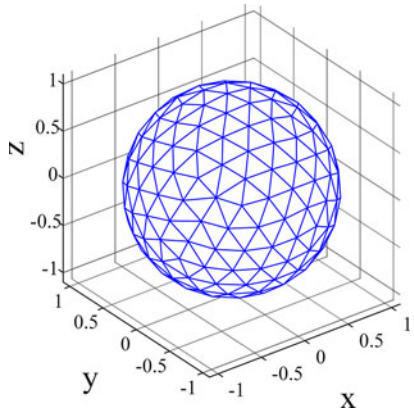

Fig. 4. Typical spherical surface formed by 200 points marking the directions of the resultant magnetic vector of the transmitter in the absence of a load (i.e., no-load condition).

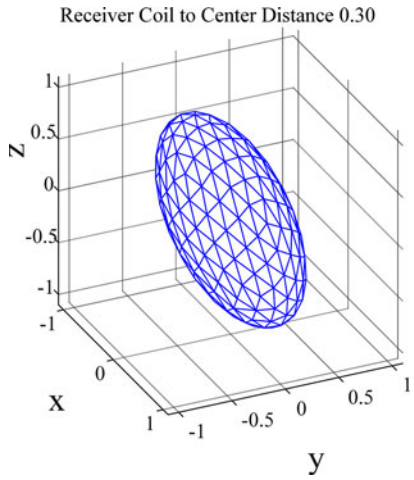

Fig. 5. Typical distorted spherical surface formed the 200 magnetic field vector positions in the presence of a load (i.e., loaded condition).

where C_v is the voltage amplitude for adjusting the total output power level.

Since the coil circuit is a resonator, the resonant frequency is $\omega_o = \frac{1}{\sqrt{LC}}$, where the coil inductance is L and lumped compensating capacitor is C.

The idea of uniform vector distribution is now illustrated with the initial assumption that a power inverter is used to drive the three orthogonal transmitter coils without current control. If 200 uniformly distributed points are used to represent the surface of the sphere, the power inverter can drive the three coil currents to generate a magnetic field vector (5) that can point at these 200 points to form such spherical surface. Since the magnetic field vector is formed by the currents in the three orthogonal transmitter coils, this approach applies to both series and parallel compensated coil resonators in principle. Under a no-load condition, this no-load surface is a perfectly spherical as shown in Fig. 4. In the presence of a load, the power flows in the direction toward the load, this loaded surface will be distorted from an ideal sphere as shown in Fig. 5.

Let the coordinates of the *h*th point of the reference (no-load) surface point on the ideal reference sphere be denoted as

$$P_{R_h} = (x_{R_h}, y_{R_h}, z_{R_h}) = (I_{mx_h}, I_{my_h}, I_{mz_h}) \quad (7)$$

where the three currents are captured at point-*h* under no-load conditions.

The corresponding coordinates of the loaded surface point of the distorted sphere can be denoted as

$$P_{L_h} = (x_{L_h}, y_{L_h}, z_{L_h}) = (I_{mx_h}, I_{my_h}, I_{mz_h}) \quad (8)$$

where the three currents are captured at point-*h* under loaded conditions.

If the same number of points (e.g., *N* points) are used to describe both of the no-load and loaded surfaces, the corresponding points of the magnetic field vectors under the no-load and loaded conditions have two different sets of Cartesian coordinates. The distance D_h for the *h*th point between the no-load and the loaded coordinates forms the distortion distance which can be defined as

$$D_h = \sqrt{(x_{R_h} - x_{L_h})^2 + (y_{R_h} - y_{L_h})^2 + (z_{R_h} - z_{L_h})^2}, \quad \text{for } h = 1 \text{ to } N. \quad (9)$$

Therefore, a set of *N* distortion distances can be derived as

$$\mathbf{D} = \{D_1, D_2, \ldots, D_N\}. \quad (10)$$

The distortion distance in (10) can be normalized. For the *h*th distortion distance (d_h), it can be defined as

$$d_h = \frac{D_h}{\sum_{X=1}^{N} D_X}. \quad (11)$$

The above analysis [(7)–(11)] is based on the assumption that the power inverter is used to drive the transmitter coils without tight current control. Compared with the no-load condition (which forms an ideal no-load spherical surface with *N* points), the loaded condition will lead to a change of current magnitudes in the three transmitter coils. So the loaded currents will generate a distorted spherical surface (i.e., the loaded surface is distorted from an ideal spherical surface). The most distorted regions of the loaded surface correspond to the areas through which most of the power flows. Therefore, scanning the vector to the *N* distributed points using the power inverter without a tight current control provides a mechanism to detect the directions of the targeted loads. The distortion distance is proportional to the power absorbed. Based on the use of the magnetic field vectors, the distorted regions of the loaded surface provide information of the required power flow directions if voltage-control mode is used.

In Section IV, it will be shown that the current-control mode is the preferred method because 1) it is a direct current control method and 2) it allows one to determine the power vectors for all of the *N* points directly. Therefore, the power requirements for the *N* directions can be determined based on the transmitter coil current and voltage information without using the distortion distance concept. A weighted time-sharing scheme is proposed based on the information of these power vectors in Section IV.

III. Analysis of Omnidirectional WPT Systems Using Current Amplitude Control

The omnidirectional wireless energy transfer system under consideration has three orthogonal transmitter coils for single and multiple receivers. The current-voltage relationship can be derived from the Kirchhoff's voltage law equation (12) as shown at the bottom of the next page where subscripts *x*, *y*, and *z* refer to the three orthogonal coils of the transmitter; subscript L_X refers to the receiver coil of the *x*th load; $R_x + jX_x = R_x + j\omega L_x + \frac{1}{j\omega C_x}$ is the total impedance of the *x*th circuit; R_x, L_x, and C_x refers to the resistance, inductance, and capacitance, respectively, of the *x*th circuit; M_{i-j} is the mutual inductance between coil i and j; I_n and V_n are the current and source voltage, respectively, of each resonator in the root-mean-square phasor form

$$v_n(t) = \sqrt{2} V_n e^{j\omega t} \quad (13)$$

$$i_n(t) = \sqrt{2} I_n e^{j\omega t}. \quad (14)$$

Note that for the load resonators, i.e., the power receivers, the source voltage is zero

$$V_{L_1} = V_{L_2} = \ldots = V_{L_n} = 0. \quad (15)$$

Now consider the situation that there is only one receiver in the system. Equation (12) is reduced to

$$\begin{cases} V_x = I_x (R_x + jX_x) + j\omega M_{x-L_1} I_{L_1} \\ V_y = I_y (R_y + jX_y) + j\omega M_{y-L_1} I_{L_1} \\ V_z = I_z (R_z + jX_z) + j\omega M_{z-L_1} I_{L_1} \\ 0 = j\omega M_{x-L_1} I_x + j\omega M_{y-L_1} I_y + j\omega M_{z-L_1} I_z \\ \qquad + (R_{L_1} + jX_{L_1}) I_{L_1}. \end{cases} \quad (16)$$

By multiplying each term on both sides of (16) with the corresponding $\bar{I}$, (16) becomes

$$\begin{cases} V_x \cdot \overline{I_x} = I_x (R_x + jX_x) \cdot \overline{I_x} + j\omega M_{x-L_1} I_{L_1} \cdot \overline{I_x} \\ V_y \cdot \overline{I_y} = I_y (R_y + jX_y) \cdot \overline{I_y} + j\omega M_{y-L_1} I_{L_1} \cdot \overline{I_y} \\ V_z \cdot \overline{I_z} = I_z (R_z + jX_z) \cdot \overline{I_z} + j\omega M_{z-L_1} I_{L_1} \cdot \overline{I_z} \\ 0 = j\omega M_{x-L_1} I_x \overline{I_{L_1}} + j\omega M_{y-L_1} I_y \overline{I_{L_1}} + j\omega M_{z-L_1} \\ \qquad I_z \overline{I_{L_1}} + (R_{L_1} + jX_{L_1}) I_{L_1} \overline{I_{L_1}}. \end{cases} \quad (17)$$

Taking the sum of the first three equations gives

$$\begin{aligned} & V_x \overline{I_x} + V_y \overline{I_y} + V_z \overline{I_z} \\ & = |I_x|^2 (R_x + jX_x) + |I_y|^2 (R_y + jX_y) + |I_z|^2 (R_z + jX_z) \\ & + j\omega M_{x-L_1} I_{L_1} \overline{I_x} + j\omega M_{y-L_1} I_{L_1} \overline{I_y} + j\omega M_{z-L_1} I_{L_1} \overline{I_z}. \end{aligned} \quad (18)$$

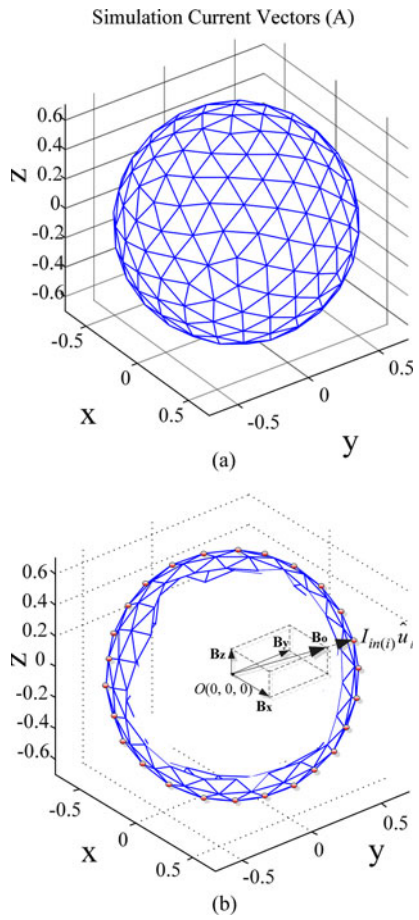

Fig. 6. (a) Simulated current vectors plotted in 3-D space. (b) *i*th current vector plotted in 3-D space.

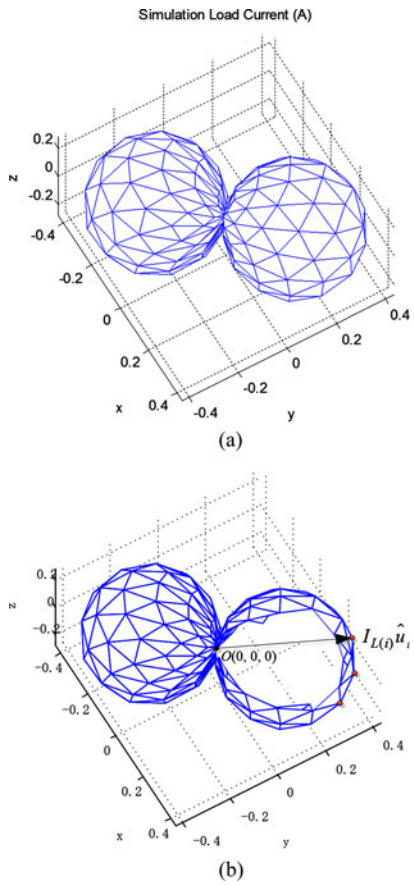

Fig. 7. (a) Simulated load current. (b) *i*th load current vector plotted in space.

The conjugate of the forth equation in (17) is

$$\begin{aligned} 0 &= (-j\omega M_{x-L_1})\overline{I_x} I_{L_1} + (-j\omega M_{y-L_1})\overline{I_y} I_{L_1} \\ &\quad + (-j\omega M_{z-L_1}\overline{I_z} I_{L_1}) + (R_{L_1} - jX_{L_1})\,\overline{I_{L_1}} I_{L_1} \\ &\quad j\omega M_{x-L_1}\overline{I_x} I_{L_1} + j\omega M_{y-L_1}\overline{I_y} I_{L_1} + j\omega M_{z-L_1}\overline{I_z} I_{L_1} \\ &\quad = (R_{L_1} - jX_{L_1})\,\overline{I_{L_1}} I_{L_1}. \end{aligned} \tag{19}$$

Thus

$$\begin{aligned} V_x\overline{I_x} + V_y\overline{I_y} + V_z\overline{I_z} &= |I_x|^2 (R_x + jX_x) + |I_y|^2 (R_y + jX_y) \\ &\quad + |I_z|^2 (R_z + jX_z) + |I_{L_1}|^2 (R_{L_1} - jX_{L_1}). \end{aligned} \tag{20}$$

The real power in the system is equal to the real part of (20)

$$\begin{aligned} P_{\text{real}} &= \Re\left(V_x\overline{I_x} + V_y\overline{I_y} + V_z\overline{I_z}\right) = |I_x|^2 R_x + |I_y|^2 R_y \\ &\quad + |I_z|^2 R_z + |I_{L_1}|^2 R_{L_1} = P_{\text{loss}} + P_{\text{load}}. \end{aligned} \tag{21}$$

The efficiency of the wireless energy transfer system is equal to

$$\begin{aligned} \eta &= \frac{|I_{L_1}|^2 R_{L_1}}{|I_x|^2 R_x + |I_y|^2 R_y + |I_z|^2 R_z + |I_{L_1}|^2 R_{L_1}} \\ &= 1 - \frac{|I_x|^2 R_x + |I_y|^2 R_y + |I_z|^2 R_z}{P_{\text{real}}} = 1 - \frac{P_{\text{loss}}}{P_{\text{real}}} \end{aligned} \tag{22}$$

where

$$P_{\text{loss}} = |I_x|^2 R_x + |I_y|^2 R_y + |I_z|^2 R_z. \tag{23}$$

$$\begin{bmatrix} R_x + jX_x & 0 & 0 & j\omega M_{x-L_1} & \cdots & j\omega M_{x-L_n} \\ 0 & R_y + jX_y & 0 & j\omega M_{y-L_1} & \cdots & j\omega M_{y-L_n} \\ 0 & 0 & R_z + jX_z & j\omega M_{z-L_1} & \cdots & j\omega M_{z-L_n} \\ j\omega M_{L_1-x} & j\omega M_{L_1-y} & j\omega M_{L_1-z} & R_{L_1} + jX_{L_1} & \cdots & j\omega M_{L_1-L_n} \\ \vdots & \vdots & \vdots & \vdots & \ddots & \vdots \\ j\omega M_{L_n-x} & j\omega M_{L_n-y} & j\omega M_{L_n-z} & j\omega M_{L_n-L_1} & \cdots & R_{L_n} + jX_{L_n} \end{bmatrix} \begin{bmatrix} I_x \\ I_y \\ I_z \\ I_{L_1} \\ \vdots \\ I_{L_n} \end{bmatrix} = \begin{bmatrix} V_x \\ V_y \\ V_z \\ V_{L_1} \\ \vdots \\ V_{L_n} \end{bmatrix} \tag{12}$$

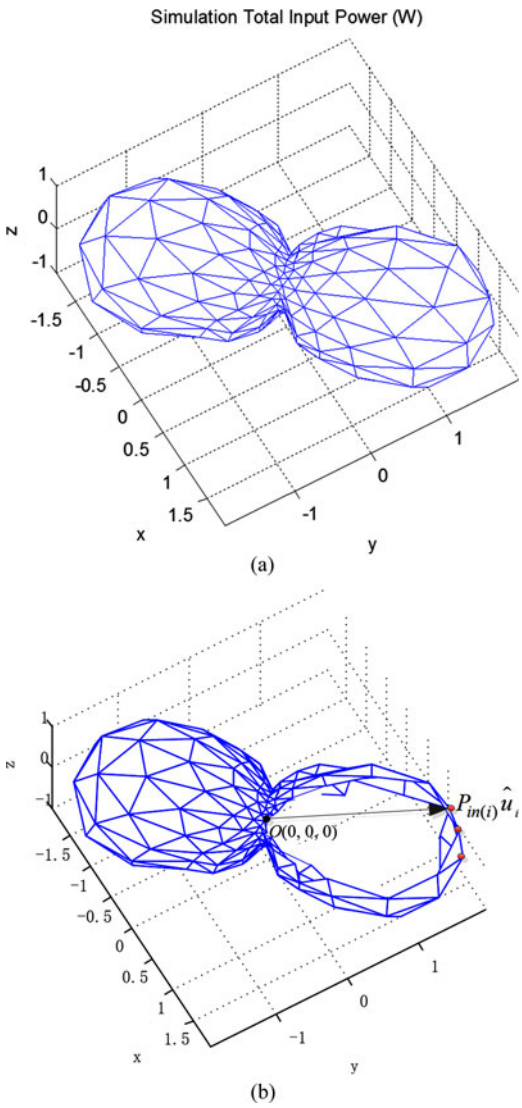

Fig. 8. (a) Simulated total input power. (b) *i*th input power vector plotted in space.

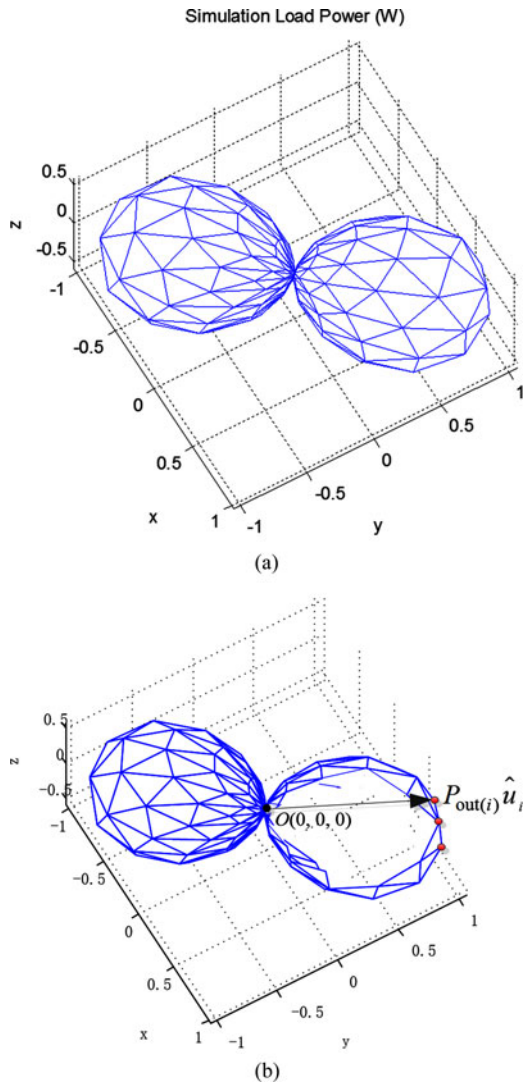

Fig. 9. (a) Simulated load power. (b) *i*th output power vector plotted in 3-D space.

Practically, the series resistances of the three transmitting coils R_x, R_y, and R_z are mainly due to the ac resistance of the coils. Since the three coils are about the same size, the series resistances can be regarded as the same

$$R_0 \cong R_x \cong R_y \cong R_z. \tag{24}$$

If the transmitter current is driven according to (4), the power loss in the system is a constant value

$$P_{\text{loss}} = C_i^2 R_0. \tag{25}$$

To deliver the most power to the receiver with the same limit of current output from the power source, all the vectors in whole sphere vector set $\mathbf{P_n}$ are scanned for a small period of time. The averaged real power during firing each vector is recorded for comparison, and the vector with the greatest real power output is the optimized direction of firing the magnetic field

$$\Re\left(V_x\overline{I_x} + V_y\overline{I_y} + V_z\overline{I_z}\right) = C_i^2 R_0 + P_{\text{load}}. \tag{26}$$

When there are multiple loads, (26) can be extended as

$$\Re\left(V_x\overline{I_x} + V_y\overline{I_y} + V_z\overline{I_z}\right) = C_i^2 R_0 + P_{L_1} + P_{L_2} + \ldots + P_{L_n}. \tag{27}$$

However, measuring the real output power on the power supply side provides the total load power but no information about the power-sharing ratios among the loads. Receiver (secondary) circuits should have power management control for the loads, such as the charging control circuit for a battery load.

IV. Power Flow Control Through a Weighted Time-Sharing Scheme

In order to enhance the power delivery performance, a new method is proposed. The power delivered to the *N* points can be determined first. Then, according to the power demand, a weight time-sharing scheme is proposed.

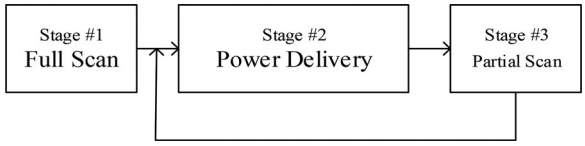

Fig. 10. Scanning and power control flowchart.

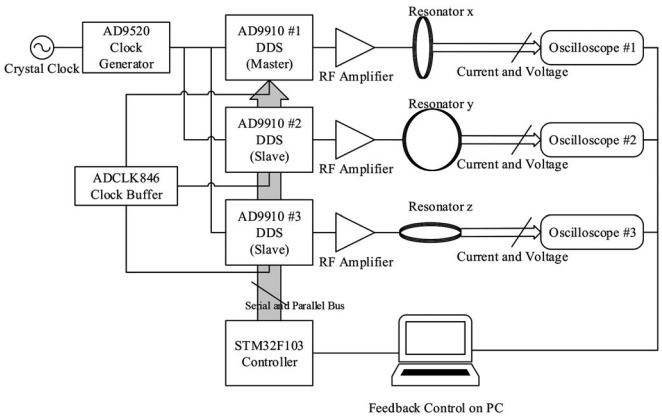

Fig. 11. Schematic of the experimental setup.

A. Input Current "Vector"

In Fig. 6(a), each node represents an input current "vector" $\mathbf{I}_{\text{in}(i)}$, which has three components: I_x, I_y, and I_z, with the same frequency and phase, and $\sqrt{I_x^2 + I_y^2 + I_z^2} = I^2$, where I is a constant value. In 3-D space as shown in Fig. 6(a), a node with coordinates $(I_x, I_y, I_z)$is used to represent three current components I_x,I_y, I_z for coil-*x*, coil-*y*, and coil-*z*, respectively. Since the magnitude of the vector for each node being the same, we choose 200 nodes (i.e., $N = 200$) uniformly distributed in a spherical surface to do the simulation and experiments. Fig. 6(b) shows the *i*th node and the input current vector with magnitude *I*, and direction defined by unit vector $\hat{u}$, where

$$\widehat{u_i} = \left(\frac{I_{xi}}{I}, \frac{I_{yi}}{I}, \frac{I_{zi}}{I}\right) \tag{28}$$

and

$$\mathbf{I}_{\text{in}(i)} = I_{\text{in}(i)}\widehat{u_i}. \tag{29}$$

B. Load Current "Vector"

In Fig. 7(a), each node represents a load current "vector" $\mathbf{I}_{L(i)} = I_{L(i)}\widehat{u_i}$, with magnitude $I_{L(i)}$, and direction $\widehat{u_i}$, where $I_{L(i)}$is the value of load current when the transmitter is excited by $\mathbf{I}_{in(i)}$ defined in (29) and $\widehat{u_i}$ is the unit vector defined in (28), as shown in Fig. 7(b).

C. Input Power "Vector"

In Fig. 8(a), each node represents an input power "vector" $\mathbf{P}_{\text{in}(i)} = P_{\text{in}(i)}\widehat{u_i}$, with magnitude $P_{\text{in}(i)}$, and direction $\widehat{u_i}$, where $P_{\text{in}(i)}$ is the sum of input power at coil-*x*, coil-*y*, and coil-*z*

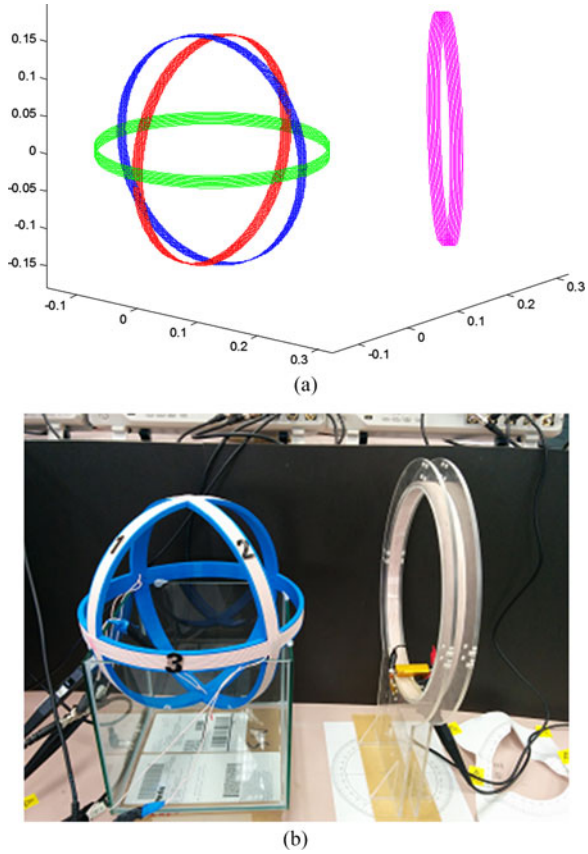

Fig. 12. (a) Simulation model. Red, blue, green, and violate coils stand for transmitter *x*, *y*, *z*, and load coil, respectively. (b) Experiment allocation. The coils are placed exactly the same location as the simulation model.

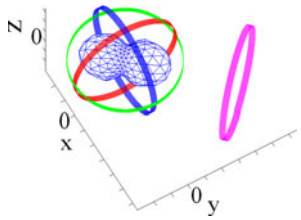

Fig. 13. Relative positions of the transmitter coils and receiver coil for the single load tests (including a typical vector plot insider the transmitter coils).

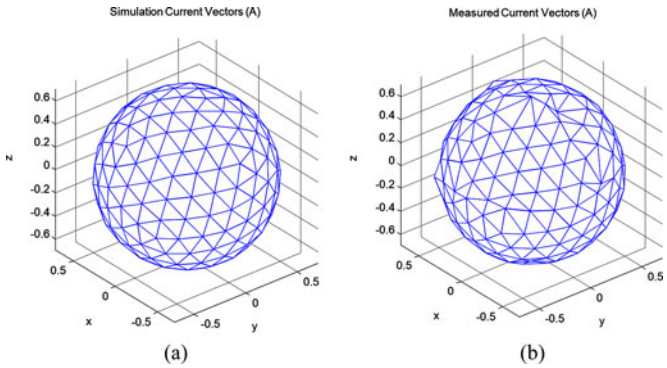

Fig. 14. (a) Simulated transmitter current vectors plotted in 3-D space. (b) Measured transmitter current vectors plotted in 3-D space.

TABLE I
MEASURED VALUES OF INPUT CURRENT, INPUT VOLTAGE, INPUT POWER, OUTPUT CURRENT, OUTPUT VOLTAGE, AND OUTPUT POWER

I_x		V_x		I_y		V_y	
Magnitude (A)	Phase Angle (Deg)	Magnitude (V)	Phase Angle (Deg)	Magnitude (A)	Phase Angle (Deg)	Magnitude (V)	Phase Angle (Deg)
0.18	181.34	3.61	155.95	0.67	182.68	8.22	118.47
I_z		V_z		I_{out}		V_{out}	
Magnitude (A)	Phase Angle (Deg)	Magnitude (V)	Phase Angle (Deg)	Magnitude (A)	Phase Angle (Deg)	Magnitude (V)	Phase Angle (Deg)
0.11	181.71	2.57	109.05	0.45	131.86	6.03	170.44
P_{in}				$P_{out}(W)$			
$P_{in_x}(W)$	$P_{in_y}(W)$	$P_{in_z}(W)$	$P_{in_{total}}(W)$	1.07			
0.29	1.21	0.04	1.54				

TABLE II
PARAMETERS IN THE SYSTEM

Name	Symbol	Value
Turns of the coils	N	11
Radius of the wire cross section	ρ	0.75 mm
Diameter of the coils	d	30 cm
Length of the coils	l	19 mm
Center point of the three transmitting coils	$\boldsymbol{p_x}, \boldsymbol{p_y}, \boldsymbol{p_z}$	$(0, 0, 0)$, the Origin
Normal vector of coil-x	$\hat{\mathbf{n}}_x$	(1, 0, 0)
Normal vector of coil-y	$\hat{\mathbf{n}}_y$	(0, 1, 0)
Normal vector of coil-z	$\hat{\mathbf{n}}_z$	(0, 0, 1)
Self-inductance of the coils	L	83.5039 μH
Compensating Capacitance of the coils	C	1 nF
Equivalent Serial Resistance of each coil	R_0	0.72 Ω
Operation Frequency	f	$\frac{1}{2\pi\sqrt{LC}}$ Resonant Frequency

TABLE III
COLOR CODES FOR DIFFERENT COILS DEFINED IN THE LAYOUT FIGURE

Coil	Color
Transmitter Coil-x	Red
Transmitter Coil-z	Green
Receiver Coil-Load-1	Purple
Receiver Coil-Load-2	Yellow

when the transmitter is excited by $\mathbf{I}_{\text{in}(i)}$ defined in (29) and $\widehat{u_i}$ is the unit vector defined in (28), as shown in Fig. 8(b).

D. Load Power "Vector"

In Fig. 9(a), each node represents a load power "vector" $\mathbf{P}_{\text{out}(i)} = P_{\text{out}(i)}\widehat{u_i}$, with magnitude $P_{\text{out}(i)}$, and direction $\widehat{u_i}$, where $P_{\text{out}(i)}$ is the magnitude of load power when the transmitter is excited by $\mathbf{I}_{\text{in}(i)}$ defined in (29) and $\widehat{u_i}$ is the unit vector defined in (28), as shown in Fig. 9(b).

E. Weighted Time Sharing of Power Flow Control

Under the current-mode control, the power flow control method with weighted time sharing consists of three stages (see Fig. 10).

TABLE IV
ANGULAR AND POSITIONAL ARRANGEMENTS OF THE RECEIVER COILS

Angle θ (deg)	$\boldsymbol{p}_{\boldsymbol{Load}_1}$	$\boldsymbol{p}_{\boldsymbol{Load}_2}$
45	(0.3, 0, 0)	(0.2121, 0.2121, 0)
60	(0.3, 0, 0)	(0.15, 0.2598, 0)
90	(0.3, 0, 0)	(0, 0.3, 0)
120	(0.3, 0, 0)	(−0.15, 0.2598, 0)
180	(0.3, 0, 0)	(−0.3, 0, 0)

1) In the first stage, the transmitter coil currents are controlled so that the central magnetic field vector is controlled to scan over the whole spherical surface. A full scan of all of the *N* vectors are captured. The magnitudes and phases of driving currents and voltages are recorded for each vector and input power vectors can be determined. The power information of these power vectors provides the direct power flow requirements in the *N* directions. There is no need to determine the no-load and loaded surfaces as in the case of the voltage-mode control.
2) In the second stage, power is delivered to the *N* directions of the spherical surface by pointing the magnetic field vector to these positions with time proportional to the power demands determined in the first stage. In practice, the vector may not need to point at all of the *N* positions because some of these positions may have negligible power demands. The weighted time-sharing process essentially focuses the power flow toward the positions with relatively high power demands.
3) In the third stage, a partial scan is performed in order to check if there is major change in the power receiving. The partial scan covers a portion of the full spherical surface only in each cycle so as to allocate most of the time for power delivery. The full surface can be covered within several scans.
4) If the scanning process observes that the load demands in the *N* positions gradually decrease to zero, the transmitter circuit can go into sleep mode. The first stage can be

TABLE V
MUTUAL INDUCTANCES IN THE SYSTEM FOR THE FIVE ARRANGEMENTS IN TABLE IV

θ (deg)	$M_{x-\mathrm{Load}_1}$	$M_{y-\mathrm{Load}_1}$	$M_{z-\mathrm{Load}_1}$	$M_{x-\mathrm{Load}_2}$	$M_{y-\mathrm{Load}_2}$	$M_{z-\mathrm{Load}_2}$	$M_{\mathrm{Load}_1-\mathrm{Load}_2}$
45	2.579 μH	~ 0	~ 0	2.372 μH	2.361 μH	~ 0	-4.683 μH
60	2.579 μH	~ 0	~ 0	1.950 μH	2.525 μH	~ 0	-4.081 μH
90	2.579 μH	~ 0	~ 0	~ 0	2.579 μH	~ 0	-1.136 μH
120	2.579 μH	~ 0	~ 0	-1.928 μH	2.532 μH	~ 0	-0.6621 μH
180	2.579 μH	~ 0	~ 0	-2.607 μH	~ 0	~ 0	-0.4754 μH

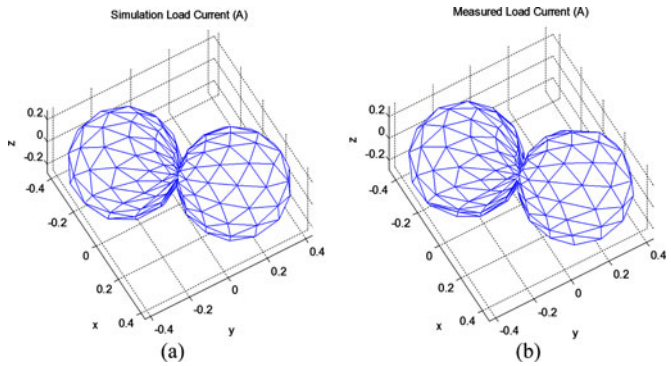

Fig. 15. (a) Simulated load current vector plot. (b) Measured load current vector plot.

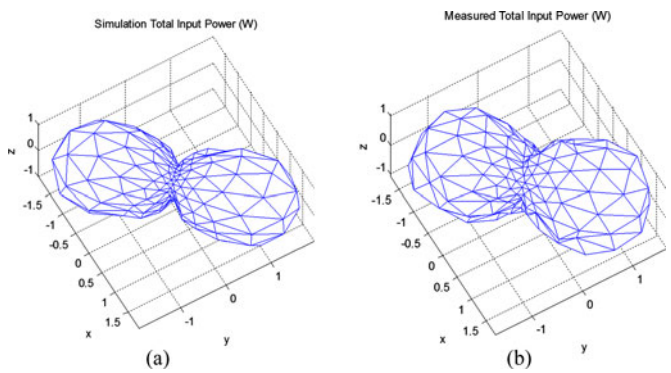

Fig. 16. (a) Simulated total input power plot. (b) Measured total input power plot.

periodically activated to check the presence of the loads. The power flow control process will start again if a load is detected.

V. SIMULATION AND EXPERIMENTAL VERIFICATION

Both simulation and experiments have been carried out to verify the proposed method of load detection and power flow control. The simulation is based on (12) and is programmed in MATLAB. Two-hundred reference vectors are generated using least energy iteration methods, each vector covering $\frac{4\pi}{200}$ sr. In order to supply the controlled currents to the three coils in the experiments, a synchronized direct digital synthesis (DDS) system is built to generate three channel amplitude and phase adjustable voltage signals feeding the RF amplifiers for power amplification. Since the preferred power driving technique is current source, an external measuring and feedback control loop using oscilloscopes and computers are used, as shown in Fig. 11.

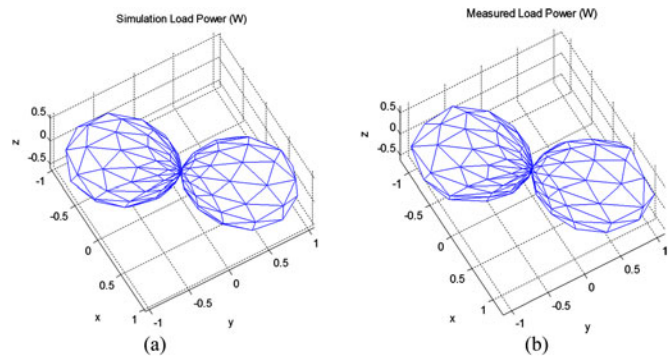

Fig. 17. (a) Simulated load power plot. (b) Measured load power plot.

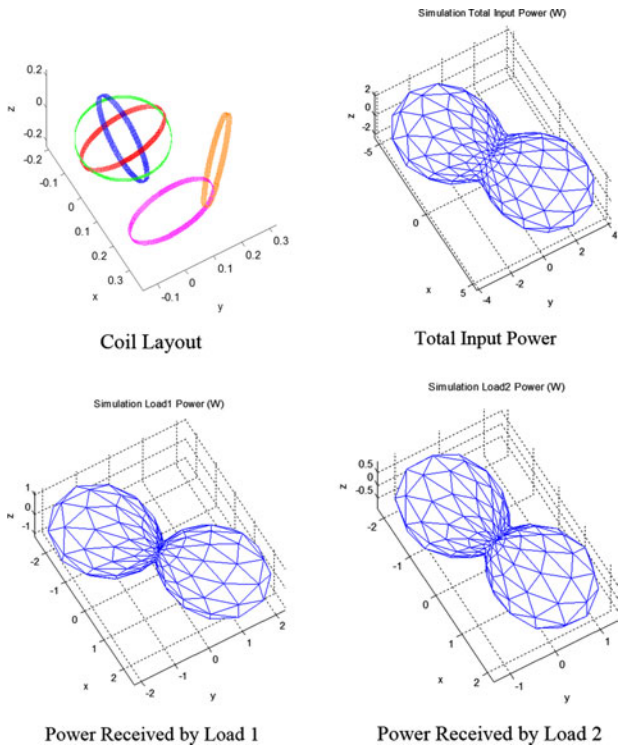

Fig. 18. Simulated results with two receiver coils with their axes having a displacement angle of 45°.

Both simulation and experiments were conducted to verify the proposed theory. The data are plotted in a way that the vectors are connected with each other to form polyhedrons for clear visual effects. Results of tests on both single load and multiple loads are included.

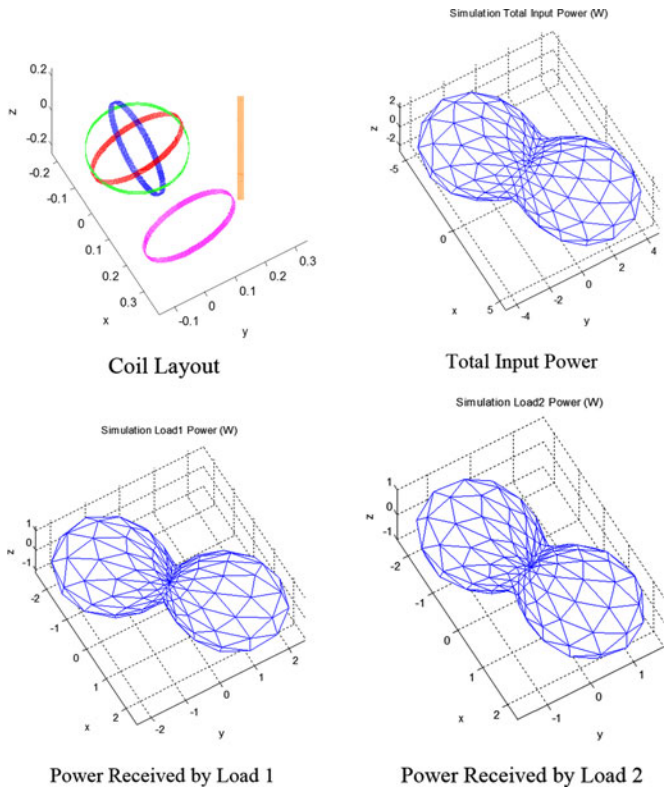

Fig. 19. Simulated results with two receiver coils with their axes having a displacement angle of 60°.

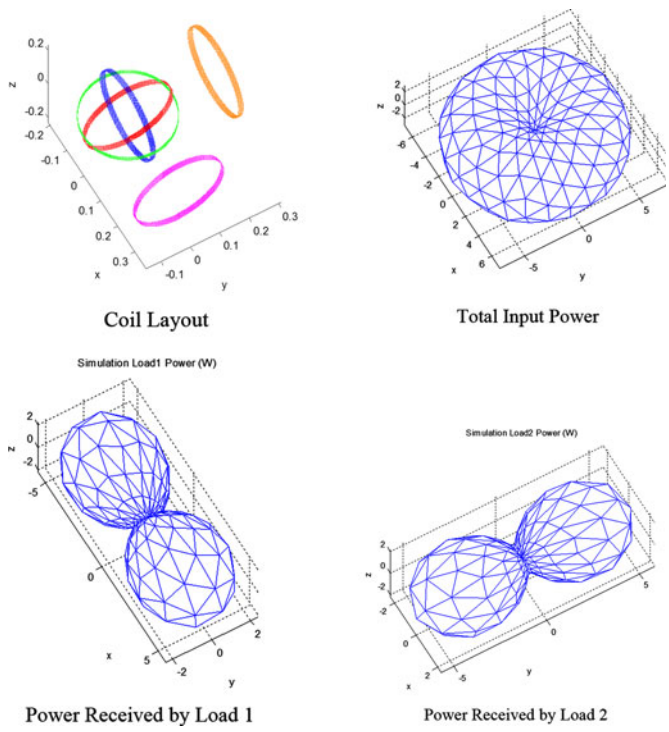

Fig. 20. Simulated results with two receiver coils with their axes having a displacement angle of 90°.

A. *Tests on Single Load*

Figs. 12(a) and (b) show the simulation setup and experimental setup, respectively, of an omnidirectional WPT system with one single load placing at (0.2121, 0.2121, 0.02 m) and the central of the receiving coil is facing at location (0, 0, 0.02 m). The coils are of the identical sizes with a diameter of 30 cm, a coil width of 1.9 cm and of 11 turns. The self-inductance of the coil is 83.5309 μH. The compensating capacitors are all 1 nF. In a particular single load test, the load resonator is placed in the position shown in Fig. 13. The following plots of the simulated and measured vectors are based on this setup. The orientations of the vector plots (as shown inside the transmitter coils in Fig. 13) are also with respect to receiver coil position.

Figs. 14(a) and (b) show the simulated and measured results of the spherical surface constructed by the 200 vector positions. As explained in the theory, the surface forms a spherical shape, indicating that the current-control mode can be used to direct the magnetic field vector toward these 200 positions. This set of results confirm the omnidirectional power control capability of the proposal. Figs. 15–17 show the corresponding simulated and measured plots of the load current vector, total input power vector, and the load power vector, respectively. Observation of these plots in the context of the relative positions in Fig. 13 indicates power flows wirelessly toward the receiver coil.

For the *i*th node as shown in Figs. 6(b) and 9(b), as an example (exactly the node *i* as shown in the figures), $\mathbf{I}_{\text{in}} = I_{\text{in}}\widehat{u}_i$,

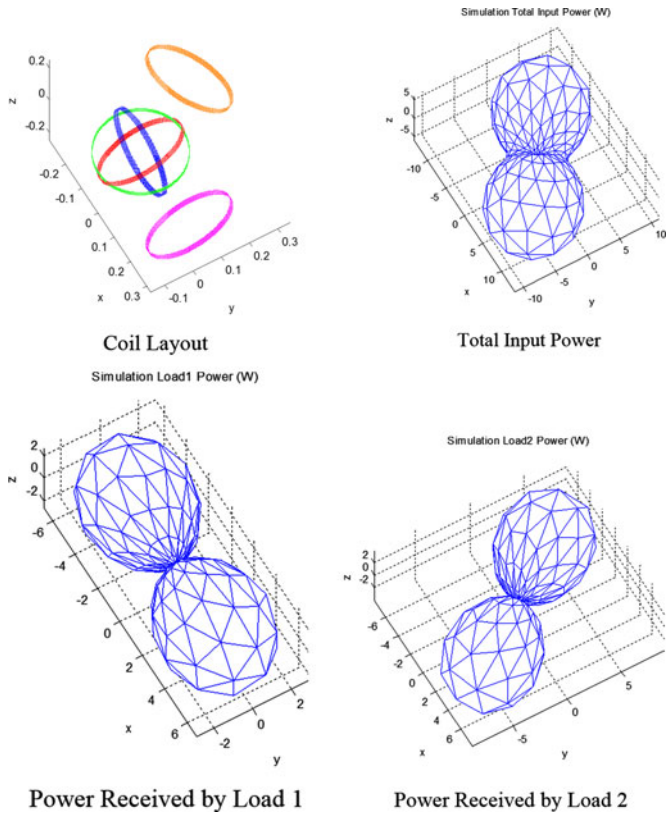

Fig. 21. Simulated results with two receiver coils with their axes having a displacement angle of 120°.

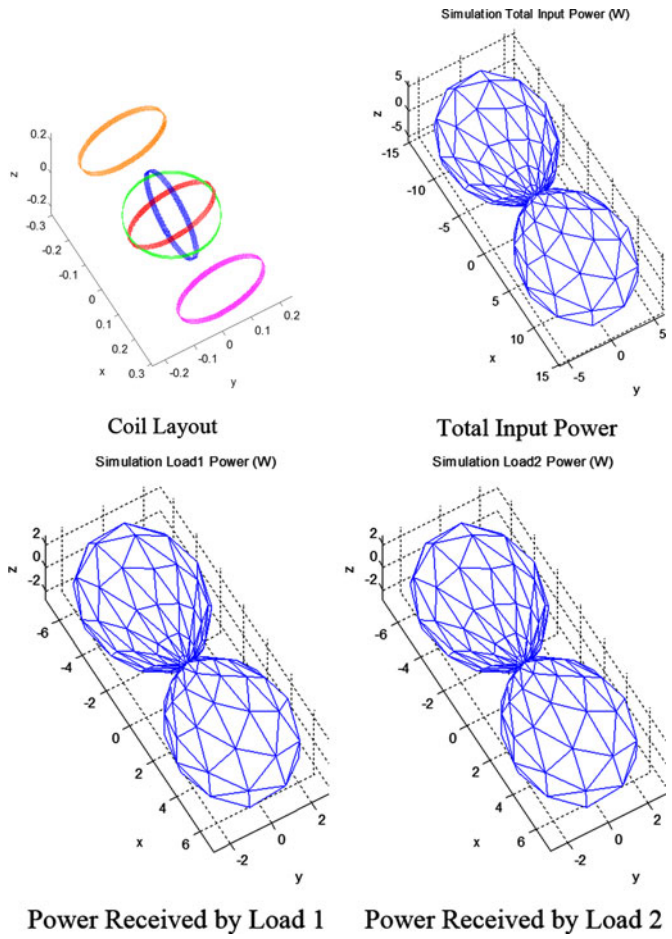

Fig. 22. Simulated results with two receiver coils with their axes having a displacement angle of 180°.

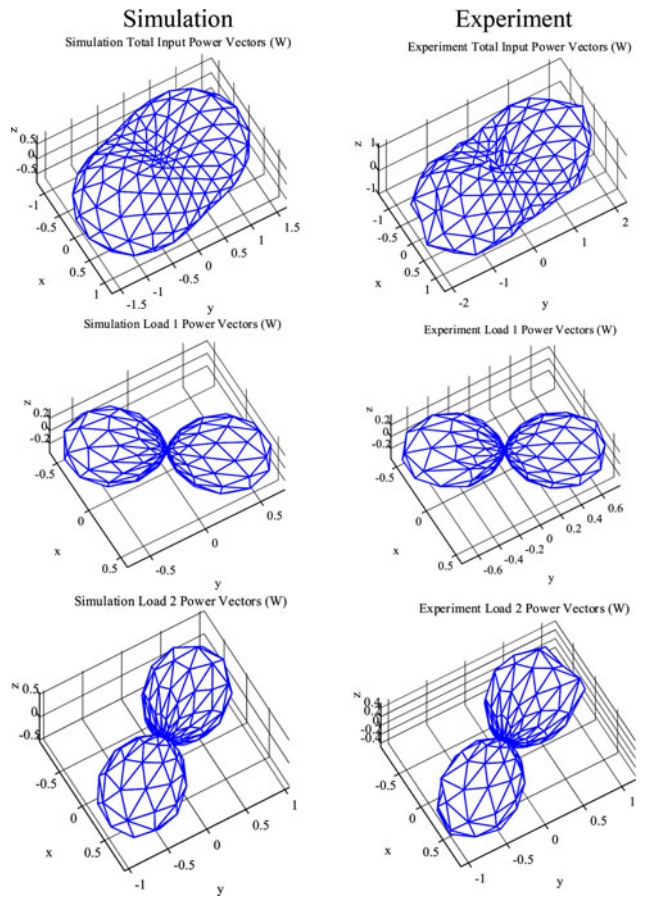

Fig. 23. Simulated and experimental results with two receiver coils with their axes having a displacement angle of 90°.

$I_{\text{in}} = 0.707$, $\hat{n} = (0.2516, 0.9551, 0.1562)$, the measured values of input current, input voltage, input power, output current, output voltage, and output power are listed in Table I. An energy efficiency of 69.5% is achieved.

B. Tests on Multiple-Load Tests

With the theory confirmed with the practical measurements, the use of the omnidirectional system for multiple loads is studied with the simulation tool and experimental evaluation. Tables II and III tabulate the technical information of the system setup. The two receiver coils are placed in five different relative positions as specified in Table IV, and the corresponding mutual inductance information for these five arrangements are provided in Table V.

1) Simulation Study on Multiple Loads: The relative locations of the two receiver coils and the simulation results of the vector plots for the total input power, power received by Load 1 and Load 2 for the angular displacement of 45°, 60°, 90°, 120°, and 180° are shown in Figs. 18–22. It is important to note from Figs. 18 and 19 that the mutual coupling between the two receiver coils does affect the power flow directions. When the two receiver coils are close (45° and 60°), the power vector plots of the Load 1 and Load 2 show that the power flow is not as direct as the single-load case in Fig. 17. However, as the angular displacement, and, hence, the relative positions between the two receiver coils increases (90°, 120°, and 180°), the mutual coupling between the two receiver coils also decreases. Consequently, the power vector plots in Figs. 20–Fig. 22show that the power flow paths point directly to the two load coils.

2) Experimental Verification: Practical tests have been conducted to verify the theoretical analysis. A set of five coil resonators have been constructed according to the parameters tabulated in Table II. It should, however, be noted that there are still some variations in the inductance and capacitance values because of the practical tolerance. Thus, while it is the aim of the practical tests to use identical coil resonators for the transmitter and receivers, some variations in their parameters are difficult to avoid.

Two sets of practical measurements with their respective simulation results are included in Figs. 23 and 24. In Fig. 23, the two receiver coils have an angular displacement of 90°. The two individual power vector plots for the two loads are measured first. The measured power vector plots generally agree with the simulated results. The combined total input power vector plot is then measured. Again, the measured input power vector plot is close to the simulated one. When the two loads are placed with an angular displacement of 120°, the simulated and experimental results are plotted in Fig. 24. Considering some parameter

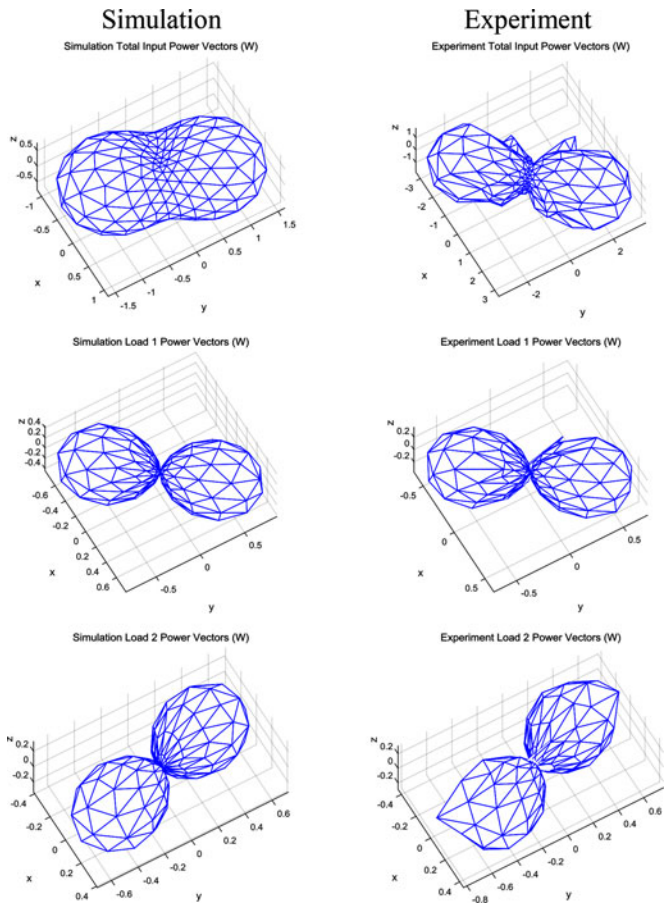

Fig. 24. Simulated and experimental results with two receiver coils with their axes having a displacement angle of 120°.

variations among the five coil resonators due to component tolerance, the experimental results agree well with the theoretical results

VI. Conclusion

This paper addresses the basic control principles of omnidirectional WPT. A new method is proposed to enable the magnetic field vector, through the current amplitude control in the three orthogonal transmitter coils, to point evenly over a spherical surface. This feature provides a truly omnidirectional power flow control for the WPT system for both single and multiple loads. Then, a power flow control method based on a weighted time-sharing scheme has been developed to deliver the power to the appropriate directions in order to improve WPT performance. A comprehensive analysis has been included to explain this omnidirectional WPT power control method. The proposed method has been successfully evaluated with simulation studies and practically confirmed with a hardware setup. While the control principle is explained and demonstrated in a 3-D omnidirectional WPT system, it can be reduced to a 2-D omnidirectional WPT system.

References

[1] N. Tesla, "Apparatus for transmitting electrical energy," U.S. Patent 1 119 732, Dec. 1, 1914.
[2] M. Hutin and M. Leblanc, "Transformer system for electric railways," U.S. Patent 5 27 857, Oct. 23, 1894.
[3] L.P. Wheeler, "Tesla's contribution to high frequency," *Electr. Eng.*, vol. 62, pp. 355–357, 1943.
[4] A. Ghahary and B. H. Cho, "Design of a transcutaneous energy transmission system using a series resonant converter," *IEEE Trans. Power Electron.*, vol. 7, no. 2, pp. 261–269, Apr. 1992.
[5] A. W. Green and J. T. Boys, "10kHz inductively coupled power transfer concept and control," in *Proc. 5th Int. Conf. Power Electron. Variable Speed Drives*, 1994, pp. 694–699.
[6] G. A. Covic and J. T. Boys, "Inductive power transfer," in *Proc. IEEE*, vol. 101, no. 6, pp. 1276–1289, Jun. 2013.
[7] S. Y. Hui, "Planar wireless charging technology for portable electronic products and Qi," *Proc. IEEE*, vol. 101, no. 6, pp. 1290–1301, Jun. 2013.
[8] J. S. Ho, S. Kim, and A. S. Y. Poon, "Midfield wireless powering for implantable systems," *Proc. IEEE*, vol. 101, no. 6, pp: 1369–1378, Jun. 2013.
[9] K. O'Brien, "Inductively coupled radio frequency power transmission system for wireless systems and devices," Ph.D dissertation, von der Fakultät Elektrotechnik und Informationstechnik, Technische Univ. Dresden, Dresden, Germany, May 2006, pp. 33–84.
[10] Z. Ouyang, Z. Zhang, M. A. E. Andersen, and O. C. Thomsen, "Four quadrants integrated transformers for dual-input isolated dc-dc converters," *IEEE Trans. Power Electron.*, vol. 27, no. 6, pp. 2697–2702, Jun. 2012.
[11] D. Wang, Y. Zhu, Z. Zhu, T. T. Mo, and Q. Huang, "Enabling multi-angle wireless power transmission via magnetic resonant coupling," in *Proc. Int. Conf. Comput. Convergence Technol.*, 2012, pp. 1395–1400
[12] O. Jonah, S. V. Georgakopoulos, and M. M. Tentzeris, "Orientation insensitive power transfer by magnetic resonance for mobile devices," presented at the IEEE Wireless Power Transfer Conf., Perugia, Italy, May 15–16, 2013.
[13] S. C. Tang and S. Y. R. Hui, "Planar printed-circuit-board transformers with effective electromagnetic interference (EMI) shielding," U.S. Patent 6 501 364, Feb. 24, 2002.
[14] S. C. Tang, S. Y. R. Hui, and H. Chung, "Evaluation of the shielding effects on printed-circuit-board transformers using ferrite plates and copper sheets," *IEEE Trans. Power Electron.*, vol. 17, no. 6, pp. 1080–1088, Nov. 2002.
[15] W. M. Ng, C. Zhang, D. Lin, and S. Y. R., Hui "Two-dimensional and three-dimensional omnidirectional wireless power transmission," *IEEE Trans. Power Electron.*, vol. 29, no. 9, pp. 4470–4474, Sep. 2014.
[16] C. Zhang, D. Lin, and S. Y. R. Hui, "Systems and methods for load position detection and power control of omni-directional wireless power transfer," PCT Patent PCT/CN2015/071543, Jan. 26, 2015
[17] J. J. Thomson, "On the Structure of the atom: An investigation of the stability and periods of oscillation of a number of corpuscles arranged at equal intervals around the circumference of a circle; with application of the results to the theory of atomic structure," *Philosoph. Mag. Series 6*, vol. 7, no. 39, pp. 237–265, 1904.

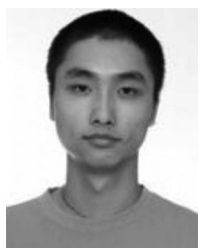

Cheng Zhang (S'13) was born in China, in 1990. He received the B.Eng. (first class Hons.) degree in electronic and communication engineering from the City University of Hong Kong, Kowloon, Hong Kong, in 2012. He is currently working toward the Ph.D. degree at the Department of Electrical and Electronic Engineering, The University of Hong Kong, Pokfulam, Hong Kong.

His current research interests include designs and optimizations for wireless power transfer applications.

Deyan Lin (M'09) was born in China, in 1972. He received the B.Sc. and M.A.Sc. degrees from the Huazhong University of Science and Technology, Wuhan, China, in 1995 and 2004, respectively, and the Ph.D. degree from the City University of Hong Kong, Kowloon, Hong Kong, in 2012.

From 1995 to 1999, he was a Teaching Assistant with the Electrical Engineering Department, Jianghan University, Wuhan, where he became a Lecturer later. From 2008 to 2009, he was a Senior Research Assistant with the City University of Hong Kong. He is currently a Postdoctoral Fellow at the Department of Electrical and Electronic Engineering, The University of Hong Kong, Pokfulam, Hong Kong. His current research interests include wireless power transfer, memristors, and modeling, control, and simulation of gas-discharge lamps.

S. Y. Hui (M'87–SM'94–F'03) received the B.Sc. (Hons) degree (Eng.) from the University of Birmingham, Birmingham, U.K., in 1984, and the D.I.C. and Ph.D. degrees from Imperial College London, London, U.K., in 1987.

He is currently the Philip Wong Wilson Wong Chair Professorship at The University of Hong Kong, Pokfulam, Hong Kong, and a part-time Chair Professorship at Imperial College London.

He has published more than 300 technical papers, including more than 200 refereed journal publications. More than 60 of his patents have been adopted by industry.

Dr. Hui is an Associate Editor of the IEEE TRANSACTIONS ON POWER ELECTRONICS and the IEEE TRANSACTIONS ON INDUSTRIAL ELECTRONICS, and an Editor of the IEEE JOURNAL OF EMERGING AND SELECTED TOPICS IN POWER ELECTRONICS. His inventions on wireless charging platform technology underpin key dimensions of Qi, the world's first wireless power standard, with freedom of positioning and localized charging features for wireless charging of consumer electronics. In November 2010, he received the IEEE Rudolf Chope R&D Award from the IEEE Industrial Electronics Society and the IET Achievement Medal (The Crompton Medal). He is a Fellow of the Australian Academy of Technology and Engineering and he also received the 2015 IEEE William E. Newell Power Electronics Award.